Check for updates

Ion irradiation to control size, composition and dispersion of metal nanoparticle exsolution†

Jiayue Wang, [ID] [a] Kevin B. Woller, [a] Abinash Kumar, [b] Zhan Zhang, [ID] [c] Hua Zhou, [c] Iradwikanari Waluyo, [ID] [d] Adrian Hunt, [ID] [d] James M. LeBeau [b] and Bilge Yildiz [ID] ⋆[ab]

Nano-engineered oxides play a frontier role in the development of next-generation catalysts and microelectronics. Recently, metal exsolution from oxides has emerged as a promising nano-structuring tool to fabricate nanoparticle-decorated oxides. However, controlling the size, density, composition, and location of exsolved nanoparticles remains a challenge, limiting the ultimate performance achievable by these nanostructures. Here, we present ion irradiation as a general platform to allow control over these parameters during metal nanoparticle exsolution, by simultaneous sputtering, implantation, and defect generation mechanisms. Using thin-film perovskite and binary oxides as model systems, we showed ion beams can controllably reduce the size of exsolved nanoparticles down to 2 nm through ion sputtering. Meanwhile, we tailored the exsolved nanoparticle composition from unitary metal to metal alloy *via* ion implantation. Furthermore, irradiation creates point defects and defect clusters, which serve as nucleation sites for metal exsolution. By leveraging this process, we tuned the density and spatial distribution of exsolved nanoparticles. Finally, we demonstrated that nanocatalysts prepared by irradiation-assisted exsolution exhibit superior catalytic activity toward water-splitting reactions than those produced using conventional exsolution methods. These findings highlight the potential of ion irradiation for engineering nanoparticle exsolution in diverse materials systems, with broad implications for electrochemical and electronic applications.

Broader context

Nanomaterials play a pivotal role in enabling next-generation energy and environmental technologies, but achieving precise nano-engineering has remained a challenge. One recent breakthrough is to synthesize nanoparticle-decorated oxides through a process termed "exsolution", wherein metallic nanoparticles precipitate out of host oxides upon reduction treatment. Through exsolution, researchers have successfully created nanostructured oxides with novel catalytic and transport properties, leading to remarkable progress in clean energy conversion and energy-efficient computing devices. Nonetheless, existing exsolution strategies are limited by their reliance on specific host metal oxides, which restricts their applicability to a narrow range of materials. Consequently, there is a strong motivation to develop a more universal and oxide-independent method for controlling exsolution. In this study, we leverage ion irradiation as an external stimulus to enable precise control of metal nanoparticle exsolution. Through ion–matter interactions, we have successfully engineered the size, composition, density, and location of the exsolved nanoparticles across various materials systems. The resulting nanostructures achieved through irradiation-assisted exsolution exhibited significantly enhanced catalytic activity for water-splitting reactions, surpassing those synthesized using conventional exsolution methods. These exciting findings highlight the potential of irradiation-assisted exsolution as a powerful platform for nano-engineering, with broad implications for energy and environmental applications.
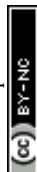
Introduction

[a] *Department of Nuclear Science and Engineering, Massachusetts Institute of Technology, Cambridge, MA 02139, USA. E-mail: byildiz@mit.edu*
[b] *Department of Materials Science and Engineering, Massachusetts Institute of Technology, Cambridge, MA 02139, USA*
[c] *Advanced Photon Source, Argonne National Laboratory, Lemont, IL 60439, USA*
[d] *National Synchrotron Light Source II, Brookhaven National Laboratory, Upton, NY 11973, USA*
† Electronic supplementary information (ESI) available. See DOI: **https://doi.org/10.1039/d3ee02448b**

Developing advanced methods to synthesize stable, active, and cost-efficient nanomaterials is critical to modern technologies.[1] A recent advance in this regard is to prepare nanostructured oxides in a phase precipitation process termed "exsolution".[2–4] In exsolution, the to-be-exsolved metal cations are first dissolved in the host oxide as dopants, forming a metal oxide solid solution. Then, upon a single-step reductive[5,6] or oxidative[7,8] treatment, metal cations phase precipitate out of the host

5464 | *Energy Environ. Sci.*, 2023, **16**, 5464–5478

This journal is © The Royal Society of Chemistry 2023

oxides as well-dispersed metal nanoparticles. Due to the simple processing and broad applications, exsolution has powered advances in the performance of electrochemical and electronic devices. For example, by exsolving nanoparticles on the oxide surface, researchers have prepared nanocatalysts with exceptional (electro)chemical stability[9] and self-regeneration capabilities[6,10] for clean energy and fuel conversion.[11,12] By exsolving nanoparticles in the bulk of oxides, self-assembled oxide nanocomposites with unique transport,[13] redox,[14] and magnetic[15] properties were achieved for next-generation electrochemical and electronic devices.

With the promising applications described above, there is substantial motivation in the field to gain better control over exsolution to realize its full potential. Today's nanoparticle exsolution often results in unitary metal particles of 10s nm size.[2,3] Since ultrafine (e.g., sub-5 nm)[16,17] and multi-element[18] nanoparticles can have higher catalytic activities, it is desirable to exsolve nanoparticles with tunable composition (multicomponent) and with tunable (reduced) size. Researchers have tried various methods, such as doping,[19,20] plasma treatment,[21,22] and electrochemistry[23,24] (see Table S1, ESI† for a more comprehensive summary) to tailor exsolution. While significant progress has been made, most strategies proposed thus far still rely on choosing a specific host oxide composition for metal exsolution.[19,20,25] Such oxide-dependent exsolution approach can have two limitations. First, due to the phase stability limit, the choice of host oxides is often constrained.[25] Second, the ideal oxide composition for exsolution may not possess other critical properties that are required in electrochemical applications, such as electronic and ionic conductivities.[12] Therefore, developing an exsolution method that is independent from the host oxide can present advantages in obtaining higher levels of functionality.

In this study, we present a flexible and oxide-independent approach to engineer metal nanoparticle exsolution, using transition-metal ion irradiation (Fig. 1a). Ion beam techniques have been widely used in semiconductor manufacturing for decades.[26] Recently, ion irradiation has also emerged as an effective tool for tailoring oxides' functionalities,[27] including ferroelectricity,[28] catalytic activity,[29] and metal-insulator transition.[30] Since ion irradiation is an external stimulus, it does not require specific host oxides and can be applied to diverse materials systems. Specifically, we hypothesize that metal ion beams can be an effective platform for metal nanoparticle exsolution via ion–matter interactions; i.e., defect formation, implantation, and sputtering, see Fig. 1b. First, irradiation modifies the type and concentration of defects in host oxides,[31] and these radiation-induced defects can tailor the location and density of exsolved nanoparticles via the defect-mediated anion/cation diffusion[32] and nanoparticle nucleation.[33] Secondly, by tuning the beam energy and dose, we can implant the to-be-exsolved metal into host oxides at specific depth[34] and at concentrations above the thermodynamic limits[35] to tailor the composition of exsolved nanoparticles. Thirdly, ion sputtering can downsize the surface exsolved nanoparticles in a progressive and well-controlled manner.[36]

To validate these hypotheses, we systematically investigated the metal exsolution behavior as a result of Ni and Cu ion beam irradiation on model binary and perovskite oxide thin films. Based on Stopping and Range of Ions in Matter (SRIM)[37] simulations, we chose to investigate the irradiation effects from 10 keV and 150 keV ions. First, as shown in Fig. 1c, ions in the 10–150 keV energy range have the highest surface sputtering yield. Therefore, by using 10 and 150 keV ion beams, we can effectively examine the ion sputtering effect on modifying the size of the exsolved nanoparticles. Secondly, as shown in Fig. 1d and Fig. S1 (ESI†), 10 and 150 keV ion beams have considerably different penetration depths, with 10 keV ions being implanted much closer to the surface. Therefore, by comparing the "surface-doping" 10 keV and the "bulk-doping" 150 keV ions, we can examine the role of ion implantation depth in modulating the composition of surface and bulk nanoparticle exsolution. In this paper, we employed the tandem accelerator to generate 10 keV and 150 keV transition metal ion beams, with the experimental setup shown in Fig. 1e. For a consistent comparison, both thermal and irradiation-assisted exsolutions were induced with identical environmental conditions in the same chamber (see Methods).

Using the methods described above, we first examined the irradiation effect on $SrTi_{0.65}Fe_{0.35}O_3$ (STF) due to its technical relevance as electrode materials in fuel cells and electrolyzers.[38,39] Previous studies have shown that STF can exsolve metallic Fe nanoparticles upon reduction of this material.[40,41] In accordance with our hypotheses, we found that Ni irradiation can downsize the surface exsolved nanoparticles on STF to 2 nm in radius and change their compositions from unitary Fe to bimetallic Fe–Ni alloy. In addition to the surface, irradiation-induced defects also promoted bulk exsolution[14,15] in STF. As a result, the irradiation-modified STF demonstrated superior activity toward alkaline oxygen evolution reactions (OER) than the conventional thermally exsolved STF. We further demonstrated that Ni irradiation can promote nanoparticle exsolution on binary oxides (ceria and zirconia) and enhance their reactivity toward high-temperature H_2O splitting. Finally, by varying the local irradiation dose, we have achieved mm-scale spatial control of exsolution on $La_{0.6}Sr_{0.4}FeO_3$ (LSF) thin films. These exciting findings highlight the utility of ion irradiation in tailoring nanoparticle exsolution to fabricate well-controlled nanocatalysts and functional oxide nanocomposites for a broad range of applications.

Results & discussion

Ion sputtering reduces the size of surface exsolved nanoparticles

We first examine the ion sputtering effect on tailoring the size of surface exsolved nanoparticles on (001)-oriented epitaxial STF thin films (Fig. 1f). Fig. 2a–c shows the top-view scanning electron microscopy (SEM) images and the corresponding radii histograms of the surface nanoparticles on the thermally exsolved, 5×10^{15} cm^{-2} 150 keV Ni-irradiated,

This journal is © The Royal Society of Chemistry 2023

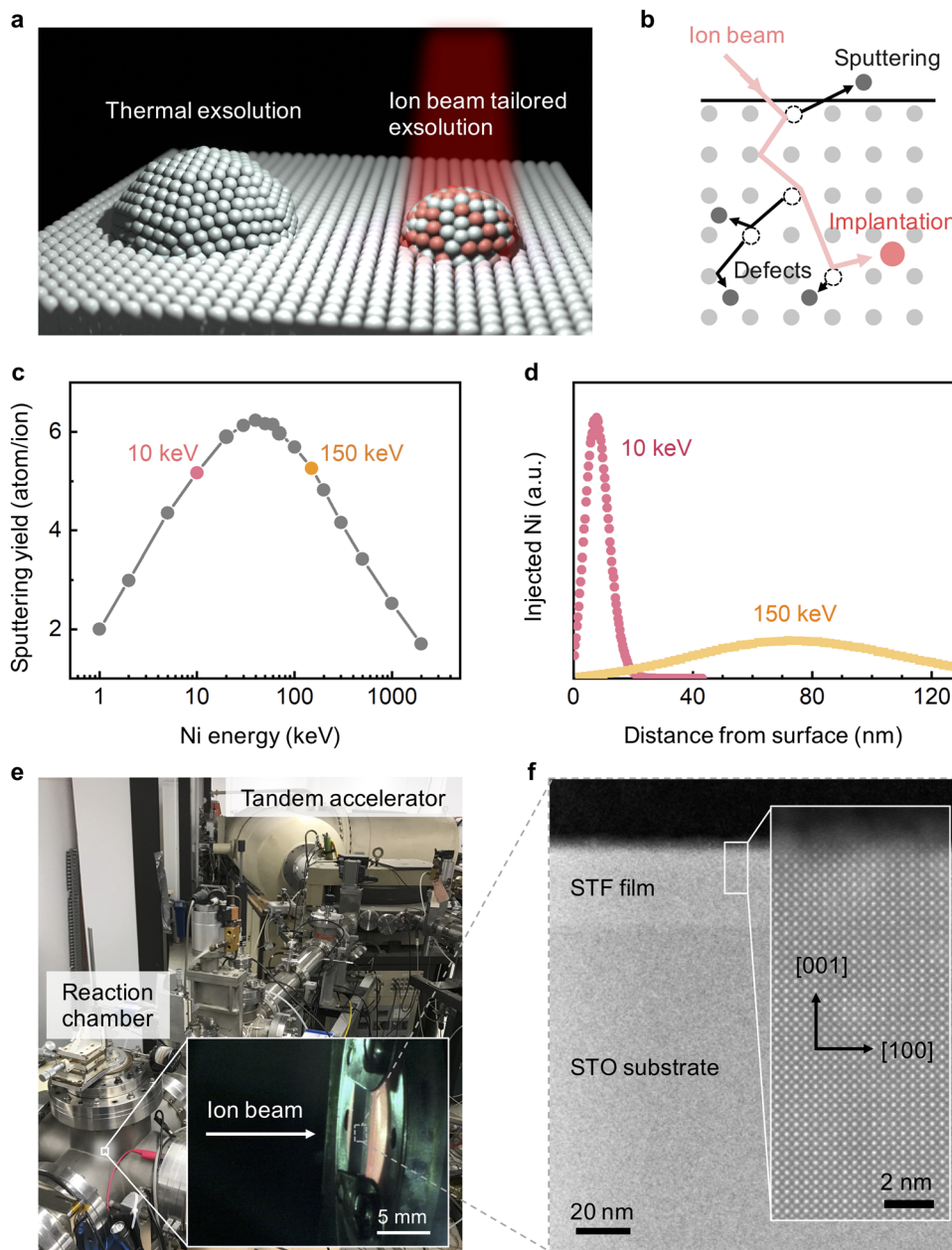*Energy Environ. Sci.*, 2023, **16**, 5464–5478 | **5465**

Fig. 1 Goal and experimental design. (a) Schematics of using an ion beam to tailor the size and composition of exsolved nanoparticles at specific locations in oxides. (b) Three types of ion–matter interactions, defect formation, implantation, and sputtering can play a role in the resulting exsolution. (c) Energy dependence of sputtering yields for a Fe target bombarded with Ni ions at normal incidence, calculated by SRIM. Note that both 10 and 150 keV Ni ions have high sputtering yields. (d) Simulated Ni profile along the irradiation direction (*i.e.*, normal incidence) in $SrTiO_3$ (STO) for both 10 and 150 keV Ni ions. Note that 10 keV Ni is more surface-sensitive than 150 keV Ni. (e) The experimental setup is coupled to a tandem accelerator for *in situ* ion irradiation during nanoparticle exsolution. (f) Cross-sectional high-angle annular dark-field scanning transmission electron microscopy (HAADF-STEM) image showing the as-prepared STF thin film on the (001)-oriented STO substrate. The zoom-in plot highlights the [001] orientation of the STF film.

and 5×10^{15} cm^{-2} 10 keV Ni-irradiated STF films. The average sizes and density of surface exsolved nanoparticles at different irradiation conditions are summarized in Fig. 2d, e and Fig. S2, S3 (ESI†).

We have found that ion irradiation can reduce the particle size. As shown in Fig. 2d and Fig. S4 (ESI†), the size of surface nanoparticles on STF can be controllably reduced by increasing the Ni irradiation dose. In particular, at a dose of 5×10^{15} cm^{-2}, 10 keV Ni irradiation reduced the average particle

radius to ∼2 nm, which are among the smallest values reported in the literature thus far for exsolved metal nanoparticles (Table S1, ESI†). Moreover, these ultrafine nanoparticles are also stable upon 20-hour thermal annealing at 800 °C (Fig. S5, ESI†), a desirable trait for high-temperature electrochemical applications such as solid fuel cells and electrolyzers.[12]

The nearly identical nucleation density across all irradiation conditions (Fig. 2e) suggests that the reduced particle size (Fig. 2d) is not a result of increased nucleation sites *via*

5466 | *Energy Environ. Sci.*, 2023, **16**, 5464–5478

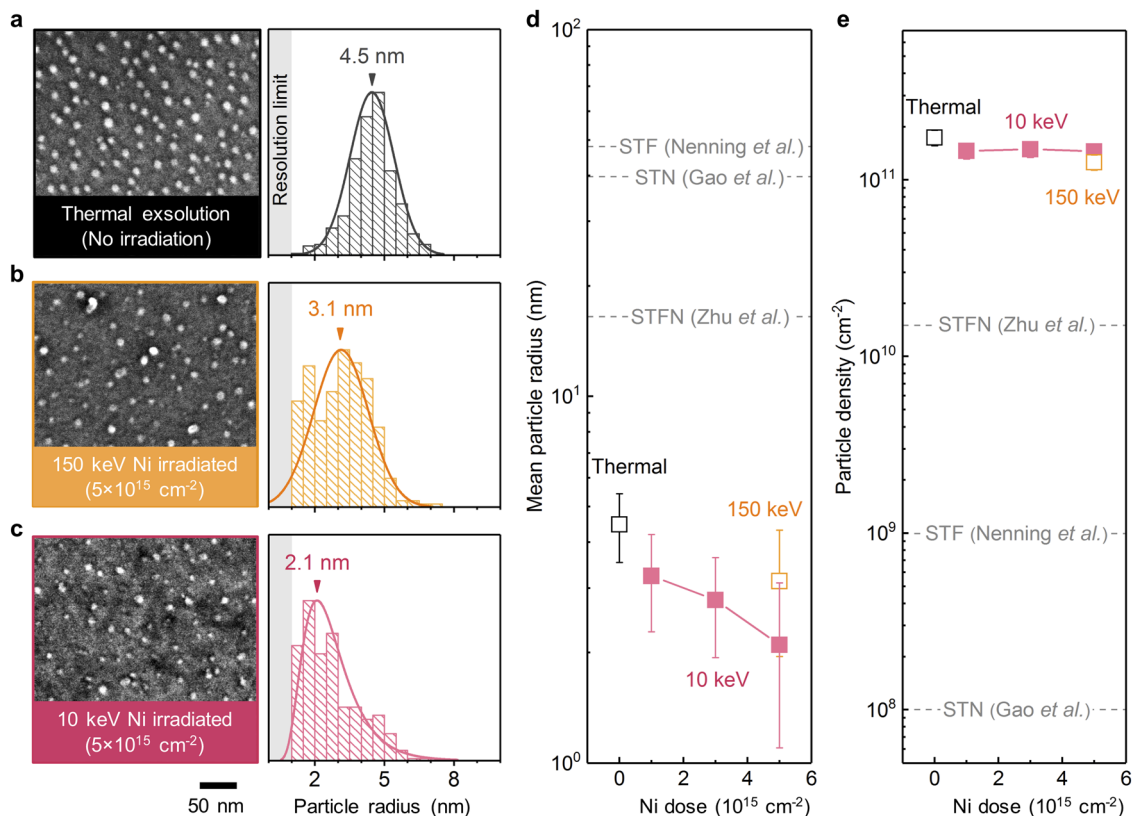This journal is © The Royal Society of Chemistry 2023

Fig. 2 Effect of Ni irradiation in tailoring particle size and density on epitaxial STF films. (a–c) Top-view SEM images and the corresponding radii histograms of the surface nanoparticles on the (a) thermally exsolved, (b) 5×10^{15} cm^{-2} 150 keV Ni-irradiated, and (c) 5×10^{15} cm^{-2} 10 keV Ni-irradiated STF films. The arrows in the radii histograms indicate the mean values, while the shaded regions indicate the resolution limit in the SEM imaging and analyses. (d) and (e) Evolution of the (d) mean particle radii and (e) particle densities as a function of 10 keV and 150 keV Ni irradiation. Note that the mean particle radius decreased with prolonged Ni irradiation, while the particle density is largely invariant. In addition, the exsolved nanoparticles on the epitaxial STF films in this study also have smaller sizes than those generated on polycrystalline STF, Ni-doped STO (STN), and Ni-doped STF (STFN) surfaces (dashed lines, adapted from ref. 45–47).
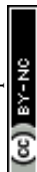
irradiation-induced defect creation. Instead, the observed particle shrinkage upon ion irradiation should primarily originate from the removal of surface atoms through ion sputtering.[36] Therefore, these observations validate our hypothesis that ion sputtering can effectively reduce the size of surface exsolved nanoparticles.

We also observed that even the thermally exsolved nanoparticles on our epitaxial STF films were significantly smaller than those reported in literature for polycrystalline samples (Fig. 2d), and had orders of magnitude higher particle density (Fig. 2e). This difference can be attributed to two main factors: the single-crystalline surface structure[41] and the fast temperature ramp rate of 200 °C min^{-1} (Fig. S6, ESI†). In the case of polycrystalline samples, surface exsolved nanoparticles preferentially nucleate along extended defects such as the grain boundaries.[42,43] For the single-crystalline surfaces in this study, however, the nanoparticle nucleation is governed by point defects,[33] which results in higher particle densities and smaller particle sizes. Additionally, the fast temperature ramp rate ensures that most nanoparticles nucleate during high-temperature annealing rather than during the ramping process (Fig. S7, ESI†), leading to an increased nucleation rate.[44]

Consequently, this further decreases the particle size and enhances the particle density.

Due to the already fast nucleation kinetics of the thermally exsolved nanoparticles on epitaxial STF films, in situ Ni irradiation did not induce a further increase in the nucleation rate on the STF surface. Consequently, the surface particle densities on STF under different irradiation conditions were very similar to the thermal exsolution case (Fig. 2e). However, it is important to note that the observed insensitivity of nanoparticle density to irradiation on epitaxial STF films does not invalidate our hypothesis that irradiation-induced defects in oxides can facilitate nanoparticle nucleation. In the forthcoming sections, we will elucidate how irradiation-induced defects can effectively promote nucleation and enhance the density of exsolved nanoparticles in the bulk (Fig. 4) as well as during surface exsolution under a slow ramp rate (Fig. 6).

To provide another reference of comparison, we also investigated the thermal exsolution characteristics of Ni-doped STF (SrTi$_{0.65}$Fe$_{0.3}$Ni$_{0.05}$O$_3$, referred to as "STFN") thin-films. As depicted in Fig. S8 (ESI†), the thermally exsolved nanoparticles on the STFN surface exhibit an average particle radius of 4 nm, which is larger than the size observed on the Ni-irradiated STF
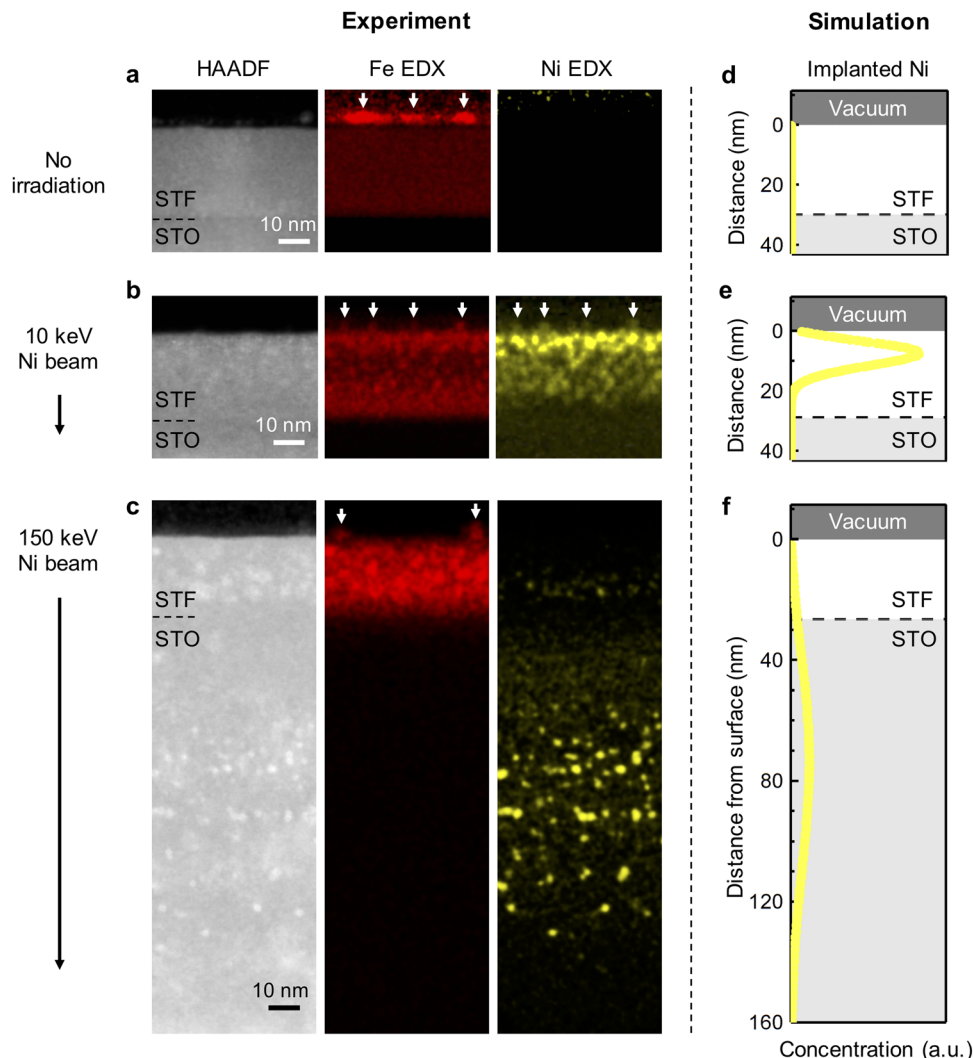
This journal is © The Royal Society of Chemistry 2023

Energy Environ. Sci., 2023, **16**, 5464–5478 | **5467**

Fig. 3 Energy-dependent Ni ion implantation in STF. Cross-sectional HAADF-STEM images and the corresponding EDX maps of the (a) thermally exsolved, (b) 5×10^{15} cm^{-2} 10 keV Ni-irradiated, and (c) 5×10^{15} cm^{-2} 150 keV Ni-irradiated STF films. The surface exsolved nanoparticles are highlighted with arrows in the EDX maps. Color intensities in the EDX maps reflect the atomic compositions. (d)–(f) The SRIM-simulated Ni implantation depth for the three cases in figures (a)–(c). Note that the Ni distribution probed by the EDX chemical mapping agrees well with the SRIM simulation. As illustrated, 10 keV Ni ions can effectively implant into the STF near-surface region, changing the surface nanoparticle composition from unitary Fe to Fe–Ni alloy. On the other hand, 150 keV Ni ions were mostly implanted into the STO substrate and hence did not change the surface nanoparticle composition.

surface. Meanwhile, the average particle density on the STFN is 7×10^{10} cm^{-2}, which is also lower than those of the Ni-irradiated STF films. Consequently, our experimental findings suggest that Ni-irradiated STF can yield finer and larger amount of exsolved nanoparticles compared to those generated through thermal exsolution in STFN.

Ion implantation tailors the composition of surface exsolved nanoparticles

To investigate the effect of ion implantation on modulating the composition of exsolved nanoparticles, we conducted chemical mapping on the thermally exsolved STF film, as well as the STF films exsolved during Ni-irradiation up to a fluence of 5×10^{15} cm^{-2} at 10 keV and at 150 keV (Fig. 3a–c). For comparison, corresponding SRIM simulations are presented in Fig. 3d–f. It

is noteworthy that the Ni distribution revealed by the energy dispersive X-ray spectroscopy (EDX) agrees well with the SRIM simulation. Specifically, 10 keV Ni ions were implanted into the STF near-surface region (with an implanted depth of about 10 nm), while the 150 keV Ni ions were mostly implanted into the STO substrate (with an implanted depth > 80 nm). Such energy-dependent Ni implantation is further confirmed with macroscopic X-ray photoelectron/absorption spectroscopy (XPS/XAS) measurements. Using surface-sensitive XPS and total electron yield (TEY) mode XAS, we show that Ni is exclusively present on the surface of 10 keV Ni-irradiated STF film (Fig. 4a, b and Fig. S9, ESI†). In contrast, for the 150 keV Ni-irradiated STF film, the deeply implanted Ni can only be probed with bulk-sensitive partial fluorescence yield (PFY) mode XAS (Fig. S11, ESI†). Using X-ray absorption near-edge
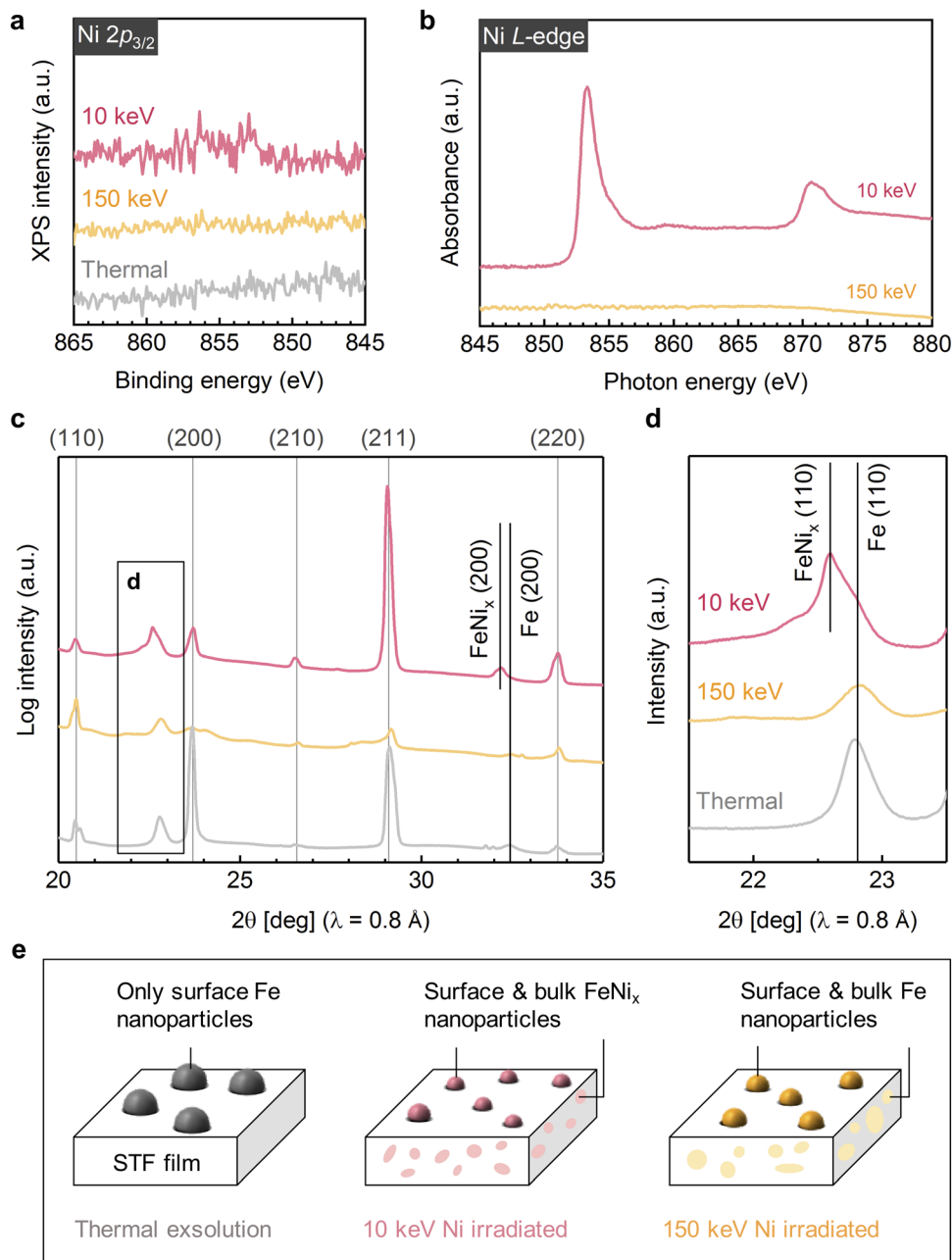
5468 | *Energy Environ. Sci.*, 2023, **16**, 5464–5478

This journal is © The Royal Society of Chemistry 2023

Fig. 4 Effect of Ni irradiation in modulating surface and bulk exsolution in STF. (a) X-ray photoelectron spectra, (b) total electron yield mode X-ray absorption spectra, and (c) and (d) Grazing incidence diffraction patterns showing the near-surface chemistry and structure of the thermally exsolved, 5×10^{15} cm^{-2} 10 keV Ni-irradiated, and 5×10^{15} cm^{-2} 150 keV Ni-irradiated STF films. (e) Schematics of the 30 nm STF film under different exsolution conditions. While thermal exsolution only generates surface Fe nanoparticles on STF, both 10 keV and 150 keV induced bulk exsolution in STF due to the ion-induced defect formation. Moreover, as 10 keV ions can effectively implant in to the STF film, it further tailors the nanoparticle composition from unitary Fe to Ni–Fe alloy (denoted as FeNi$_x$). Finally, both 10 and 150 keV Ni irradiation reduced the surface nanoparticle size due to the ion sputtering effect. The indexes labeled at the top of Fig. 4c represent the diffractions from STF/STO. The data in Fig. 4a–d are displaced vertically for better visualization.

spectroscopy (XANES), we confirm that the implanted Ni within the STF film primarily has a metallic valence state (Fig. S10, ESI†).

Having demonstrated the energy-dependent Ni implantation depth in STF, we next examine if the implanted Ni in STF can tailor the composition of surface exsolved nanoparticles.

Since the surface particles are small in volume (Fig. 2), they have low contrasts in the HAADF-STEM images.[41] Therefore, we used EDX elemental maps to locate the exsolved surface nanoparticles, which are highlighted with arrows in Fig. 3a–c. As our reference, the surface nanoparticles on the thermally exsolved STF are made of iron (Fig. 3a), which has been

This journal is © The Royal Society of Chemistry 2023

Energy Environ. Sci., 2023, **16**, 5464–5478 | **5469**

discussed in detail in our previous studies.[40,41] For the 10 keV Ni-irradiated STF film (Fig. 3b), the surface nanoparticles are enriched in both Fe and Ni while depleted in Sr and Ti (Fig. S12, ESI†), which validates our hypothesis that implanted Ni in the near-surface region can serve as the metal reservoir to tailor the composition of surface exsolved nanoparticles. On the other hand, since the 150 keV Ni ion beam was mainly implanted into the STO substrate and did not have enough temperature/time to diffuse to the STF surface, the surface nanoparticles on the 150 keV Ni-irradiated sample remained to be unitary iron (Fig. 3c and Fig. S13, ESI†).

The composition and phase of surface exsolved nanoparticles were further confirmed with the surface-sensitive and synchrotron-based grazing incidence diffraction (GID) measurements (Fig. 4c). While no metal peaks can be observed on the as-prepared STF film (Fig. S14, ESI†), clear metallic diffractions (Im-3m) can be found on both the thermally exsolved and Ni-irradiated STF (highlighted in Fig. 4d). As discussed in our previous work,[41] for the thermally exsolved STF, the metal diffraction peaks align well with the α-Fe phase (PDF#04-007-9753), which originate from the surface exsolved nanoparticles. Upon 10 KeV Ni irradiation, the metal diffraction peak shifted to a lower 2-theta position, indicating the formation of Fe–Ni alloys.[48] Therefore, in agreement with EDX mapping (Fig. 3b), GID measurements also confirm that the implanted 10 keV Ni ion can change the composition of surface nanoparticles from unitary iron to nickel-iron alloys. On the other hand, for 150 keV Ni-irradiated STF, the metal diffraction peak remains at the α-Fe position. This finding indicates that the surface nanoparticles on the 150 keV Ni-irradiated STF are unitary iron, which again agrees with the EDX results (Fig. 3c).

Irradiation-induced defects in oxides promote sub-surface exsolution

Besides the surface modification effects described above, we found that ion irradiation can also promote bulk exsolution in STF. As shown in Fig. 3a and Fig. S15, S16 (ESI†), no bulk exsolution can be observed in the thermally exsolved STF film. Nevertheless, after Ni irradiation, nanoscale Fe (Fig. 3c) or Fe–Ni (Fig. 3b) precipitates can be found in the STF sub-surface, indicating irradiation-induced bulk exsolution.

Since 150 keV Ni ions did not implant into the STF film but can still effectively promote bulk exsolution of Fe (Fig. 3c), the enhanced bulk exsolution in the Ni-irradiated STF film should mainly come from the irradiation-induced defects. Previous studies have shown that both point defects (such as oxygen vacancy[33]) and extended defects (e.g., grain boundary[43] and anti-phase boundary[49]) in host oxides can serve as preferential nucleation sites for the exsolved nanoparticles. As we did not observe noticeable extended defects in irradiated STF films (Fig. 3), we anticipate that the irradiation-induced point defects or defect clusters in the STF sub-surface to be the critical defects to promote bulk exsolution.

Like the case of surface exsolved nanoparticles, the composition of embedded nanoparticles can be also tuned by the energy-dependent ion implantation. While the embedded nanoparticles induced by the 10 keV Ni are Ni–Fe alloys (Fig. 3b and Fig. S10, S12, S17, S18, ESI†), the ones from 150 keV Ni are unitary Fe (Fig. 3c and Fig. S13, ESI†). Note that the capability to promote and tailor bulk exsolution in oxides with irradiation is desirable for (electro)catalysis and microelectronics, as it can increase the oxygen storage capability[50] and electrical conductivity[13,15] in oxides.

We have observed that the lattice parameter of STF films can be modulated through the process of Ni irradiation and implantation. As revealed by X-ray diffraction (XRD) measurements, the out-of-plane lattice parameter of STF films increased upon 10 keV Ni irradiation (Fig. S19, ESI†). The observed lattice expansion can be attributed to two potential origins. Firstly, the formation of point defects induced by irradiation in STF is a plausible reason. For instance, the creation of oxygen vacancies[39] and cation interstitials[51] is widely recognized for increasing the lattice parameter in STF. Secondly, the irradiation-induced ion implantation and bulk exsolution lead to the formation of nanoscale metal precipitates within the oxide matrix (Fig. 3b and c), which in turn could introduce strain into the host oxide lattice. Recent investigations have highlighted that embedded metal nanoparticles can induce tensile strain within the surrounding oxide matrix.[13,52,53] Given that lattice strain in oxides can enhance their electronic conductivity,[53] ionic conductivity[13,54] and surface reactivity,[52,55] the observed lattice evolution upon ion irradiation may also benefit a broad range of electrochemical applications.

Finally, based on the local and global characterization described above, we can summarize the Ni irradiation effect on STF in Fig. 4e. First, both 10 keV and 150 keV Ni ion beams help reduce the size of surface exsolved nanoparticles via ion sputtering. Second, at the moderate exsolution temperatures employed in this study, we found that only low-energy ion beams (i.e., 10 keV Ni) can effectively tailor the surface nanoparticle composition via ion implantation into the near-surface regions of the film. In contrast, high-energy ions (i.e., 150 keV Ni) are implanted into the bulk interior (Fig. 3c) and did not have enough time (and temperature) to diffuse to the surface to alloy with exsolved Fe particles. Since moderate exsolution temperatures are generally desirable to prevent nanoparticle coarsening,[56] low-energy ion beams are more effective in the compositional control of surface exsolved nanoparticles. Thirdly, both 10 and 150 keV Ni beams can generate lattice defects in the STF sub-surface, which promote bulk exsolution in STF and forms embedded, nanoscale metallic phases.

Moderate ion irradiation enhances electrocatalytic activity

We next compare the catalytic activity between the thermally exsolved and Ni-irradiated STF films. In particular, we probed the oxygen evolution reaction[57] (OER) activity of STF in an alkaline environment (1 M KOH), as a result of 10 keV Ni irradiation. As discussed earlier, 10 keV Ni irradiation reduces the size of surface nanoparticles while preserving the particle density, and changes the particle composition from unitary Fe to Fe–Ni alloy (Fig. 2, 3 and 5a). We anticipate that these

5470 | Energy Environ. Sci., 2023, **16**, 5464–5478

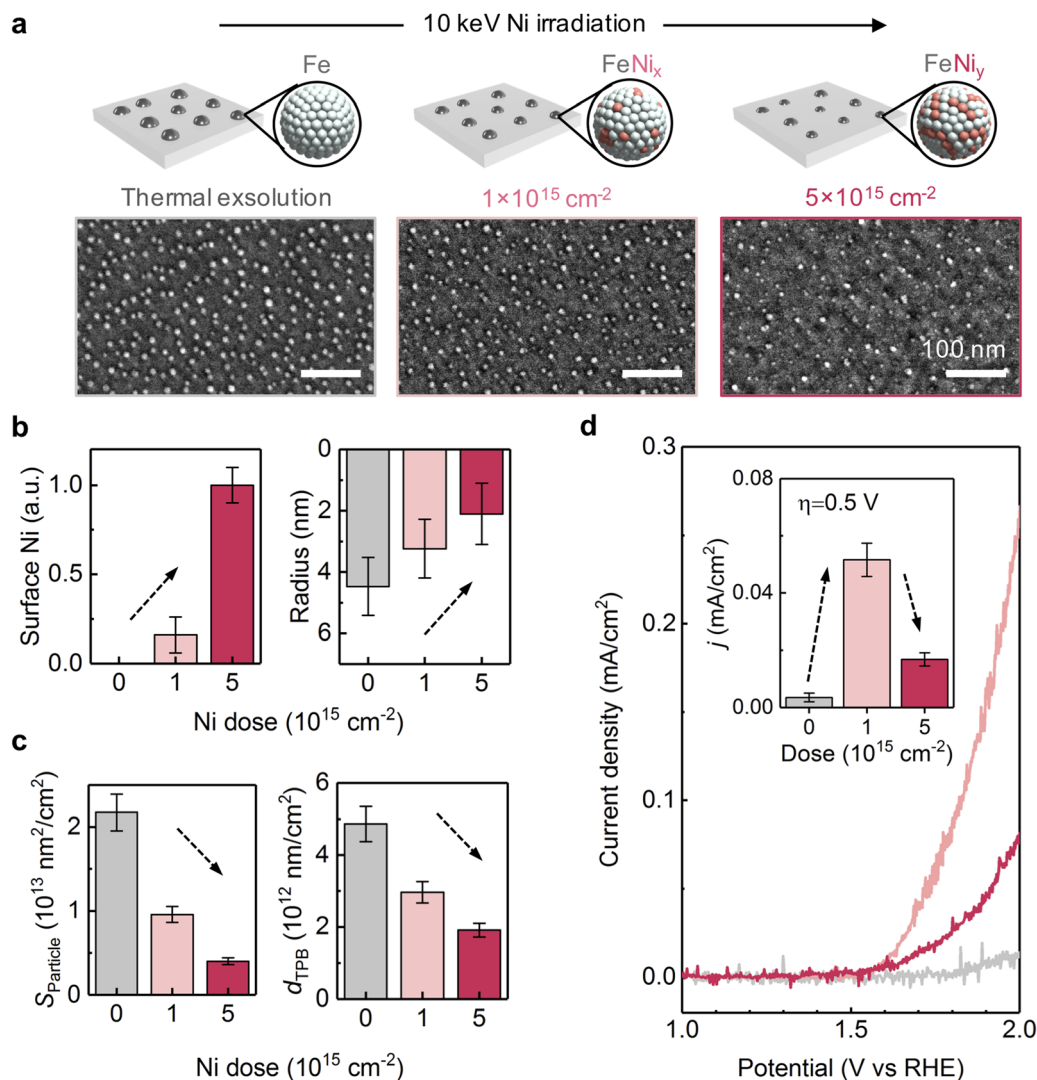This journal is © The Royal Society of Chemistry 2023

Fig. 5 Effect of Ni irradiation on the electrocatalytic activity of STF. (a) SEM images and schematics showing the impact of 10 keV Ni irradiation on surface exsolved nanoparticles – size reduction, Ni alloying, and maintenance of a relatively stable nanoparticle density. (b) Increasing the Ni dose results in a higher surface Ni concentration (quantified by XPS) and reduced nanoparticle size, which may increase the intrinsic reactivity of each active site. (c) Increased Ni dose also reduces the total surface area ($S_{Particle}$) of exsolved nanoparticles, and the density of triple phase boundaries (d_{TPB}) on the STF surface, which may reduce the number of active sites for electrocatalysis. $S_{Particle}$ and d_{TPB} were calculated based on SEM images, assuming that surface nanoparticles exhibit hemispherical geometries. (d) Linear sweep voltammetry (LSV) curves for alkaline OER on STF films at different Ni doses. The inset figure compares the current density (j) at an overpotential (η) of 0.5 V. Note that the 10 keV Ni irradiation increased the OER activity of STF at a low dose (1×10^{15} cm^{-2}), but decreased the performance at a high dose (5×10^{15} cm^{-2}).

modifications will induce two competing effects on OER: an increase in intrinsic activity by changing the composition of the particles and reducing the particle size, and a decrease in total surface area and number of active sites[58] due to ion-induced sputtering:

First, as Ni irradiation reduces the particle size and increases the surface Ni concentration by alloying (Fig. 5b), it can increase the intrinsic OER[16,18] (Fig. S20, ESI†). On the other hand, as ion sputtering reduces the particle size while maintaining the surface particle density, it can also reduce the total surface area of the catalyst particles and reduce the number of total active sites for OER. Since the surface defects on the particle[16] and particle-oxide interphases (triple phase

boundary)[59] are common active sites in oxygen evolution and oxygen reduction reactions (OER/ORR), we quantified the triple phase boundary density ($d_{TPB} = n \times 2\pi \bar{r}$) and the total particle surface area $\left(S_{Particle} = n \times 2\pi \overline{r^2} \right)$ on the STF surface as a function of Ni dose. Here n denotes surface nanoparticle density, and $\bar{r}$ represents the average radius of surface nanoparticles. As shown in Fig. 5d, both d_{TPB} and $S_{particle}$ decreased with increasing 10 keV Ni irradiation, suggesting that the total active sites for OER must decrease. Thus, due to these two competing effects of Ni irradiation on OER activity (*i.e.*, an increase in the intrinsic activity but a decrease in total active sites), we expect the optimal catalytic activity will occur at an intermediate irradiation dose.
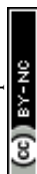
In accordance with our hypothesis, we found that the 10 keV Ni irradiation has a non-monotonic effect on STF's OER activity. First, while the thermally exsolved STF film shows negligible OER activity, 1×10^{15} cm^{-2} 10 keV Ni irradiated STF shows considerably improved OER performance (Fig. 5d). Secondly,

while low doses of Ni irradiation are beneficial for OER, we found that increasing the 10 keV Ni dose from 1×10^{15} to 5×10^{15} cm^{-2} decreases the OER activity (Fig. 5d). These findings show that by properly choosing the ion irradiation dose, irradiation-modified exsolution can have superior
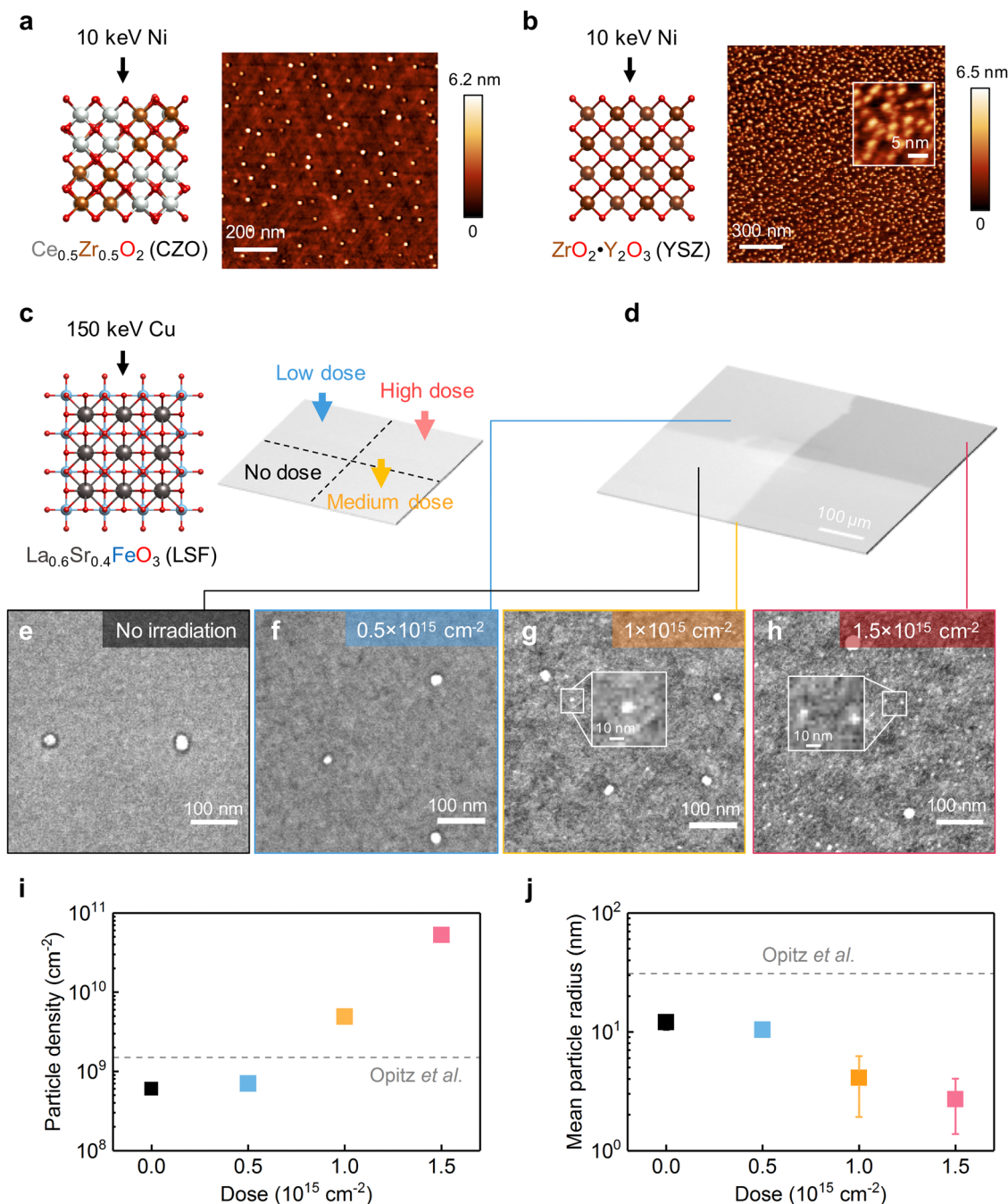
Fig. 6 Irradiation on different materials systems and local control of exsolution. (a) and (b) AFM images showing the surface morphology evolution of CZO and YSZ upon 10 keV Ni irradiation (800 °C, 1×10^{15} cm^{-2}). (c) To realize spatial control of exsolution, 150 keV Cu beams of different doses were used to irradiate different regions of one LSF sample. (d) Low magnification SEM image showing the spatially controlled ion irradiation on the LSF film. (e)–(h) High magnification SEM images showing the irradiation-enabled local control of exsolution on LSF. The inset plots in (g-h) highlight the ultrasmall nanoparticles produced by ion irradiation. (i) and (j) Comparison of the (i) particle densities and (j) average particle radii from different regions of the LSF surface, as a function of irradiation doses. The dashed lines represent the properties of thermally exsolved nanoparticles on polycrystalline LSF surfaces, adapted from ref. 23.

5472 | *Energy Environ. Sci.*, 2023, **16**, 5464–5478

This journal is © The Royal Society of Chemistry 2023

electrocatalytic performance than conventional thermal exsolution.

Irradiation on different materials systems and local control of exsolution

To demonstrate the generality of using irradiation to tailor exsolution, we continued to test this method on binary oxides. In particular, we employed 10 keV Ni beams to irradiate (111)-oriented $Ce_{0.5}Zr_{0.5}O_2$ (CZO) thin films and yttria-stabilized zirconia (YSZ) single crystals. The surface morphologies of CZO and YSZ after 10 keV Ni irradiation are shown in Fig. 6a and b. As illustrated, while the as-prepared surfaces are smooth (Fig. S21, ESI†), well-dispersed nanoparticles can be found on the surface of both materials after Ni irradiation. As a control experiment, no particles can be observed on the thermally reduced samples without irradiation (Fig. S22, ESI†), which confirms that the surface nanoparticles are induced by Ni irradiation. Along with Ni irradiation, metallic Ni (Ni^0) species started to appear on the surface (Fig. S23, ESI†). Meanwhile, no apparent surface segregation of Ce or Zr has been observed in the CZO film after Ni irradiation (Fig. S24, ESI†). These findings collectively suggest the observed surface nanoparticles are metallic Ni. To examine the catalytic activity evolution of binary oxides upon Ni irradiation, we conducted electrical conductivity relaxation (ECR) measurements[60] on the CZO films before and after Ni irradiation at 400 °C in H_2/H_2O atmospheres (Fig. S25 and S26, ESI†). As a result, we found that Ni irradiation increased the surface exchange kinetics of CZO toward H_2O splitting by four times at 400 °C (Fig. S27, ESI†). The observed irradiation-enhanced nanoparticle exsolution and (electro)catalysis on both perovskite and binary oxides thus prove that ion irradiation can be utilized to promote exsolution in a wide range of oxides to enhance their catalytic activities.

Finally, we show spatially controlled ion irradiation can be employed to tailor the local exsolution properties within a single sample. Since point defects can serve as the preferential nucleation sites for nanoparticle exsolution,[33] we hypothesize that we can effectively tailor the local density of exsolved nanoparticles by tailoring the local point defect density with irradiation. To test this hypothesis, we varied the irradiation dose on four different regions of the (001)-oriented $La_{0.6}Sr_{0.4}FeO_3$ (LSF) film (Fig. 6c). The different irradiation doses in these four different regions can be clearly visualized in SEM imaging (Fig. 6d). In particular, we chose the 150 keV Cu beam to exclude the implantation effect, as high-energy ions do not stop in the LSF film (Fig. 1d) but implant into the substrate. To further exclude the ion sputtering effect, we irradiated the LSF film prior to the thermal reduction treatment (see Methods). Therefore, by adopting the aforementioned experimental procedure, we can exclusively examine the effect of irradiation-induced defects on metal nanoparticle exsolution.

After thermal reduction treatment, the surface morphologies from the four differently irradiated regions within the same LSF sample are shown in Fig. 6e–h. As illustrated, the regions with higher irradiation doses have higher particle densities (Fig. 6i) and smaller particle sizes (Fig. 6j). In

particular, on the highly irradiated area, ultrafine nanoparticles (∼3 nm radius) started to appear on the surface (highlighted with insets in Fig. 6g and h). The appearance of these ultrafine nanoparticles clearly indicates that irradiation-induced surface defects result in additional nucleation pathways during exsolution. The reason that we have observed radiation dependence of size and density on LSF but not on STF (Fig. 2) is that here we adopted a slower ramping rate (5 °C min⁻¹ *vs.* 200 °C min⁻¹) and a lower temperature (650 °C *vs.* 800 °C) to trigger exsolution on LSF. As a result, the nucleation rate from thermal exsolution is much reduced for the LSF experiments (Fig. 6), thus allowing us to observe the irradiation-facilitated nanoparticle nucleation better.

Currently, the precise nature of the defect structure responsible for enhancing exsolution remains unclear. In our previous study, we have identified surface oxygen vacancy pairs as the preferential nucleation sites for metal exsolution on single-crystalline, (001)-oriented LSF.[33] Given that earlier finding, we expect that critical defects for nucleation of exsolution in this study, too, are linked to oxygen vacancies. This is likely the case, also because oxygen atoms have a lower threshold displacement energy in comparison to metal cations,[61] making oxygen anions more susceptible to displacement and subsequent oxygen vacancy defect formation upon irradiation. Future studies are needed to describe the atomic structure of the irradiation-induced defects in these oxides.

The findings described above prove that irradiation-induced near-surface defects can promote and tailor nanoparticle nucleation on the LSF surface during exsolution. Moreover, this proof-of-concept demonstration of using spatially controlled ion irradiation also opens new avenues for spatial control of nanoparticles. Using a micro-fabricated shadow mask or focused ion beam irradiation, we expect to leverage ion irradiation to realize much finer spatial control of nanoparticle exsolution for precise nano-architecture.

Conclusion

In summary, we present a multi-faceted, oxide-independent approach to tailor metal nanoparticle exsolution for controllable synthesis of nanocatalysts and functional oxide nanocomposites. Using binary (CZO and YSZ) and perovskite (STF and LSF) oxide thin films as model systems, we show ion irradiation can effectively tailor the size, density, composition, and location of exsolved nanoparticles. First, ion sputtering can controllably reduce the size of surface exsolved nanoparticles down to 2 nm, which are among the smallest values reported in the literature thus far. Second, implanted metal ions can tailor the composition of nanoparticles exsolved both at the surface and in the bulk, providing a convenient and direct way to synthesize exsolved nanoparticles with alloyed compositions. Third, irradiation-induced lattice defects can catalyze the nucleation of nanoparticles, and this enables controlling the density and location of exsolved nanoparticles at specific sample locations using ion irradiation. As a result, the nanostructures from

irradiation-assisted exsolution exhibited superior electrocatalytic activities toward water-splitting reactions than their counterparts prepared by conventional exsolution methods. Since ion irradiation is an external stimulus, one can apply this method to tailor exsolution in diverse materials, and not limited to a particular set of oxide hosts. Moreover, besides tandem accelerators, one can exploit other types of ion sources (such as ion implanter[30,62] and focused ion beams[34]) for practical applications and realize higher spatial resolution. Irradiation-assisted exsolution provides an effective and general platform to fabricate nanostructures with controlled size, composition and distribution, which can benefit a broad range of applications such as (electro)catalysis, nanophotonics, and electronic devices.

Methods

Sample preparation

30 nm $SrTi_{0.65}Fe_{0.35}O_3$ (STF) film was deposited using Pulsed Laser Deposition (PLD) with a KrF (λ = 248 nm) excimer laser. The STF thin films were grown onto 10 mm × 5 mm × 0.5 mm 0.7% Nb-doped $SrTiO_3$(001) single crystal substrates (MTI Corporation, 1-side polished). During the deposition, the backside substrate temperature was kept at 815 °C (which approximately corresponds to 600 °C surface temperature) in an oxygen pressure of 0.5 mTorr. The orientation and thickness of the STF film are confirmed via X-ray diffraction and reflectometry measurements (Fig. S28, ESI†). The surface morphology of the as-prepared STF film is characterized with atomic force microscopy (AFM), which shows a root mean square surface roughness of 0.1 nm (Fig. S29, ESI†). 30 nm $Ce_{0.5}Zr_{0.5}O_2$ (CZO) films were grown onto 10 mm × 5 mm × 0.5 mm yttria-stabilized zirconia (YSZ) (111) single crystal substrates (MTI Corporation, 1-side polished) with PLD. Prior to the PLD deposition, the YSZ (111) single crystal substrates were annealed in Ar at 1250 °C for 12 hours, which results in atomic-flat surfaces (Fig. S18, ESI†). During deposition, the backside substrate temperature was kept at 750 °C (which approximately corresponds to 550 °C surface temperature) in an oxygen pressure of 20 mTorr. The X-ray diffraction results for the CZO films are shown in Fig. S30 (ESI†). 20 nm $La_{0.6}Sr_{0.4}FeO_3$ (LSF) film was grown on 10 mm × 10 mm × 0.5 mm 0.7% Nb-doped $SrTiO_3$ (001) single crystal substrates (MTI Corporation, 1-side polished) using PLD (Fig. S31, ESI†). During deposition, the backside substrate temperature was kept at 850 °C (which approximately corresponds to 650 °C surface temperature) in an oxygen pressure of 20 mTorr. More detailed characterizations of the epitaxial thin films can be found in our previous studies (STF,[41] CZO,[63,64] and LSF[65]).

In situ ion irradiation during metal nanoparticle exsolution

10 keV Ni^- and 150 keV Ni^+ beams were generated with a tandem accelerator at the Cambridge Laboratory for Accelerator-based Surface Science (CLASS). The opposite charge states of ion beams are due to the different accelerating methods (Fig. S32, ESI†). For simplicity, in this paper, we do not distinguish the charge states, but use the term Ni beam to refer to both Ni^+ and Ni^-. For each irradiation experiment, the main chamber was first pumped down to 10^{-6} Torr at room temperature. The sample was then heated to 800 °C at a ramp rate of $\sim$200 °C per minute (Fig. S6, ESI†). The rapid heating ensures that a majority ($\sim$90%, see Fig. S7, ESI†) of nanoparticles were exsolved during the irradiation/annealing step, which enables ion irradiation to dynamically tailor materials' exsolution process (*e.g.*, particle nucleation and growth[33]). The high-temperature irradiation also helps avoid sample amorphization.[66] During the experiment, the incident ion beam was roughly parallel to the surface normal (*i.e.*, roughly along the [001] direction in STF, and the [111] direction in CZO and YSZ). A large aperture size (diameter = 8 mm, which is comparable to the sample geometry) was used in order to achieve a uniform irradiation dose distribution across the entire surface. During the entirety of the experiments, the pressure of the main chamber was actively maintained to be around 10^{-5} Torr. After the irradiation, the sample was naturally cooled in the same environment to 100 °C before it was taken out of the chamber. The Ni dose of each sample was controlled by adjusting the beam current, while keeping the 1 hour irradiation/annealing time fixed. For the control experiment, we prepared a thermally exsolved STF film using the exact same thermal treatment, just without ion beam irradiation. No discernible surface damage can be observed by AFM on the sample surface after Ni irradiation (Fig. S33, ESI†).

Spatially controlled ion irradiation and exsolution

150 keV Cu^+ beams from the CLASS tandem accelerator were employed for room-temperature irradiation. During the experiment, the incident ion beam was roughly parallel to the surface normal (*i.e.*, roughly along the [001] direction in LSF). A shadow mask was employed to realize spatially controlled ion irradiation (Fig. S34, ESI†). The aperture diameter was set to be 8 mm to ensure uniform irradiation within the irradiated region. During the entirety of the experiments, the pressure of the main chamber was actively maintained to be around 10^{-5} Torr. After irradiation, the sample was reduced in 200 sccm 3% H_2/N_2 at 650 °C for 5 hours to trigger exsolution, with a ramp rate of 5 °C min^{-1}.

Stopping and range of ions in matter (SRIM) simulation

In this study, we used SRIM-2013 software[37] to simulate the ion–matter interactions between the Ni beam and STF. We used a very similar composition, $SrTiO_3$ (STO), in the simulation, instead of $SrTi_{0.65}Fe_{0.35}O_3$ (STF). This is because STO has well-established threshold displacement energies,[61] which are the most critical input parameters in the SRIM simulation. In the modeling, 10 keV and 150 keV Ni ions were set to bombard the stoichiometric $SrTiO_3$ (density: 4.81 g cm^{-3}) at normal incidence, which is in accordance with the experimental setup. A total of 10^6 ions were simulated using the "monolayer collision step/surface sputtering" option. The threshold displacement energies (E_d) for Sr, Ti, and O were set to be 53.5, 65, and

5474 | *Energy Environ. Sci.*, 2023, **16**, 5464–5478

This journal is © The Royal Society of Chemistry 2023

35.7 eV, respectively. The displacement energies were chosen based on the previous molecular dynamics simulations.[61]

Soft X-ray absorption spectroscopy (XAS)

Ex situ total electron yield (TEY) mode and partial fluorescence yield (PFY) mode soft XAS measurements were performed at the IOS (23-ID-2) beamline of the National Synchrotron Light Source II (NSLS-II) at Brookhaven National Laboratory. Previous studies have shown that the electron sampling depth in the TEY-XAS measurements is smaller than ~5 nm.[67] Therefore, the electronic structure revealed by TEY-XAS in this work should directly reflect the near-surface chemistry of the STF film. On the other hand, PFY mode has a much larger probing depth (on the order of 100 nm), which can therefore reveal the sub-surface chemistry in the irradiated STF film.

Grazing incidence diffraction (GID)

Ex situ GID experiments were carried out at beamline 33-ID at the Advanced Photon Source, Argonne National Laboratory. A photon energy of 15.5 keV was used, which corresponds to a wavelength of 0.79987 Å. To obtain the signal solely from the top few nanometers of the STF film, we conducted the GID measurements at $0.06°$ incident angle, which is far below the critical angle $0.16°$, at which total reflection occurs (Fig. S35, ESI†). As such, the GID measurements are highly sensitive to the near-surface structures.

Transmission electron microscopy

Cross-sectional TEM samples of thin-film STF were prepared by either Au^+ or Ga^+ focused ion beams (FIB) using Raith VELION or FEI Helios 660 SEM/FIB, respectively. Prior to the FIB procedure, 20 nm carbon was deposited on the STF film by carbon evaporation with EMS QT150 ES to protect the surface morphology. Scanning transmission electron microscope (STEM) imaging and energy-dispersive X-ray spectroscopy (EDS) were performed with a probe-corrected Thermo Fisher Scientific Themis Z G3 Titan operated at 200 kV, with a convergence semi-angle of 19.2 mrad. The collection angle for HAADF-STEM images was 65–200 mrad.

Oxygen evolution reaction (OER) measurements

The OER measurements on thin-film samples were conducted following the methods developed by Stevens *et al.*[68] As shown in Fig. S36 (ESI†), a tinned-copper wire (GoodFellow) was attached to the backside of the Nb:SrTiO$_3$ substrate with silver paint (SPI Supplies). Then, all the tinned copper, silver paint, and the sample were covered in non-conductive and chemically inert hot glue (Gorilla). The sample treatment described above ensured that only the thin-film surfaces were actively exposed to the electrolytes, which is critical for impurity free OER analyses. All the OER tests were conducted in 1 M KOH (Sigma-Aldrich, 99.99%) electrolytes using a standard three electrode cell configuration. The carbon cloth (Engineered Fibers Technology) and Hg/HgO (CH Instruments) were employed as the counter and reference electrodes, respectively. The following equation was used to convert the potential against the Hg/HgO electrode *versus* the RHE, for 1 M KOH electrolyte:

$$E_{vs.\ RHE} = E_{vs.\ Hg/HgO} + 0.924\ V \tag{1}$$

A scan rate of 10 mV s^{-1} was employed for all the linear-scan voltammetry (LSV) measurements. Ultrahigh purity O$_2$ (Airgas) was purged into the electrolyte both prior to and during the measurements to ensure O$_2$ saturation. Finally, the iR correction was determined by the high frequency AC impedance measurements (Fig. S37, ESI†). The current densities were normalized to the surface area of the exposed STF films.

Author contributions

J. W. and B. Y. conceived the experiments. J. W. prepared the samples and analyzed the data. K. B. W. and J. W. conducted the ion beam irradiation experiments. J. W. performed the SRIM simulation. Z. Z., H. Z., and J. W. conducted the GID measurements. J. W., I. W., and A. H. conducted the XAS measurements. A. K. performed the STEM characterization under the supervisions of J. M. L. J. W. wrote the manuscript and all authors contributed to its revision. B. Y. designed and supervised the research.

Conflicts of interest

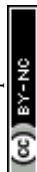There are no conflicts to declare.

Acknowledgements

This journal is © The Royal Society of Chemistry 2023

Energy Environ. Sci., 2023, **16**, 5464–5478 | **5475**

References

1 N. Baig, I. Kammakakam and W. Falath, Nanomaterials: a review of synthesis methods, properties, recent progress, and challenges, *Mater. Adv.*, 2021, **2**, 1821–1871, DOI: **10.1039/D0MA00807A**.

2 K. Kousi, C. Tang, I. S. Metcalfe and D. Neagu, Emergence and Future of Exsolved Materials, *Small*, 2021, **17**, 2006479, DOI: **10.1002/smll.202006479**.

3 J. H. Kim, *et al.*, Nanoparticle Ex-solution for Supported Catalysts: Materials Design, Mechanism and Future Perspectives, *ACS Nano*, 2021, **15**, 81–110, DOI: **10.1021/acsnano.0c07105**.

4 D. Neagu, *et al.*, Roadmap on exsolution for energy applications, *J. Phys.: Energy*, 2023, **5**, 031501, DOI: **10.1088/2515-7655/acd146**.

5 D. Neagu, G. Tsekouras, D. N. Miller, H. Ménard and J. T. S. Irvine, In situ growth of nanoparticles through control of non-stoichiometry, *Nat. Chem.*, 2013, **5**, 916–923, DOI: **10.1038/nchem.1773**.

6 Y. Nishihata, *et al.*, Self-regeneration of a Pd-perovskite catalyst for automotive emissions control, *Nature*, 2002, **418**, 164–167, DOI: **10.1038/nature00893**.

7 W. Fan, *et al.*, Anodic Shock-Triggered Exsolution of Metal Nanoparticles from Perovskite Oxide, *J. Am. Chem. Soc.*, 2022, **144**, 7657–7666, DOI: **10.1021/jacs.1c12970**.

8 M. Liang, *et al.*, A New Durable Surface Nanoparticles-Modified Perovskite Cathode for Protonic Ceramic Fuel Cells from Selective Cation Exsolution under Oxidizing Atmosphere, *Adv. Mater.*, 2022, **34**, 2106379, DOI: **10.1002/adma.202106379**.

9 D. Neagu, *et al.*, Nano-socketed nickel particles with enhanced coking resistance grown in situ by redox exsolution, *Nat. Commun.*, 2015, **6**, 8120, DOI: **10.1038/ncomms9120**.

10 H. Lv, *et al.*, In Situ Investigation of Reversible Exsolution/Dissolution of CoFe Alloy Nanoparticles in a Co-Doped Sr2Fe1.5Mo0.5O6−δ Cathode for CO2 Electrolysis, *Adv. Mater.*, 2020, **32**, 1906193, DOI: **10.1002/adma.201906193**.

11 S. Mitchell, R. Qin, N. Zheng and J. Pérez-Ramírez, Nanoscale engineering of catalytic materials for sustainable technologies, *Nat. Nanotechnol.*, 2021, **16**, 129–139, DOI: **10.1038/s41565-020-00799-8**.

12 J. T. S. Irvine, *et al.*, Evolution of the electrochemical interface in high-temperature fuel cells and electrolysers, *Nat. Energy*, 2016, **1**, 15014, DOI: **10.1038/nenergy.2015.14**.

13 S. J. Dalton and D. Neagu, A Model for Modulating Oxide Ion Transport with Endo-Particles for Application in Energy Conversion, *Adv. Energy Sustainability Res.*, 2022, **3**, 2200054, DOI: **10.1002/aesr.202200054**.

14 K. Kousi, D. Neagu, L. Bekris, E. I. Papaioannou and I. S. Metcalfe, Endogenous Nanoparticles Strain Perovskite Host Lattice Providing Oxygen Capacity and Driving Oxygen Exchange and CH4 Conversion to Syngas, *Angew. Chem., Int. Ed.*, 2020, **59**, 2510–2519, DOI: **10.1002/anie.201915140**.

15 J. Wang, *et al.*, Exsolution Synthesis of Nanocomposite Perovskites with Tunable Electrical and Magnetic Properties, *Adv. Funct. Mater.*, 2022, **32**, 2108005, DOI: **10.1002/adfm.202108005**.

16 Z. Zhuang, *et al.*, Oxygen Evolution on Iron Oxide Nanoparticles: The Impact of Crystallinity and Size on the Overpotential, *J. Electrochem. Soc.*, 2021, **168**, 034518, DOI: **10.1149/1945-7111/abef47**.

17 M. Haruta, Size- and support-dependency in the catalysis of gold, *Catal. Today*, 1997, **36**, 153–166, DOI: **10.1016/S0920-5861(96)00208-8**.

18 M. Yu, G. Moon, E. Bill and H. Tüysüz, Optimizing Ni–Fe Oxide Electrocatalysts for Oxygen Evolution Reaction by Using Hard Templating as a Toolbox, *ACS Appl. Energy Mater.*, 2019, **2**, 1199–1209, DOI: **10.1021/acsaem.8b01769**.

19 J.-S. Jang, *et al.*, Dopant-Driven Positive Reinforcement in Ex-Solution Process: New Strategy to Develop Highly Capable and Durable Catalytic Materials, *Adv. Mater.*, 2020, **32**, 2003983, DOI: **10.1002/adma.202003983**.

20 S. A. Horlick, Y.-L. Huang, I. A. Robinson and E. D. Wachsman, Controlling exsolution with a charge-balanced doping approach, *Nano Energy*, 2021, **87**, 106193, DOI: **10.1016/j.nanoen.2021.106193**.

21 V. Kyriakou, *et al.*, Plasma Driven Exsolution for Nanoscale Functionalization of Perovskite Oxides, *Small Methods*, 2021, **5**, 2100868, DOI: **10.1002/smtd.202100868**.

22 H. Khalid, *et al.*, Rapid Plasma Exsolution from an A-site Deficient Perovskite Oxide at Room Temperature, *Adv. Energy Mater.*, 2022, **12**, 2201131, DOI: **10.1002/aenm.202201131**.

23 A. K. Opitz, *et al.*, Understanding electrochemical switchability of perovskite-type exsolution catalysts, *Nat. Commun.*, 2020, **11**, 4801, DOI: **10.1038/s41467-020-18563-w**.

24 J.-h Myung, D. Neagu, D. N. Miller and J. T. S. Irvine, Switching on electrocatalytic activity in solid oxide cells, *Nature*, 2016, **537**, 528–531, DOI: **10.1038/nature19090**.

25 M. Kothari, *et al.*, Platinum incorporation into titanate perovskites to deliver emergent active and stable platinum nanoparticles, *Nat. Chem.*, 2021, **13**, 677–682, DOI: **10.1038/s41557-021-00696-0**.

26 J. M. Poate and K. Saadatmand, Ion beam technologies in the semiconductor world (plenary, *Rev. Sci. Instrum.*, 2002, **73**, 868–872, DOI: **10.1063/1.1428782**.

27 X. Xiang, *et al.*, Applications of Ion Beam Irradiation in Multifunctional Oxide Thin Films: A Review, *ACS Appl. Electron. Mater.*, 2021, **3**, 1031–1042, DOI: **10.1021/acsaelm.0c01071**.

28 S. Saremi, *et al.*, Enhanced Electrical Resistivity and Properties via Ion Bombardment of Ferroelectric Thin Films, *Adv. Mater.*, 2016, **28**, 10750–10756, DOI: **10.1002/adma.201603968**.

29 Y. Wang, *et al.*, Ion-irradiation of catalyst and electrode materials for water electrolysis/photoelectrolysis cells, rechargeable batteries, and supercapacitors, *Mater. Adv.*, 2022, **3**, 7384–7405, DOI: **10.1039/D2MA00547F**.

5476 | *Energy Environ. Sci.*, 2023, **16**, 5464–5478

This journal is © The Royal Society of Chemistry 2023

30 H. Guo, *et al.*, Strain Doping: Reversible Single-Axis Control of a Complex Oxide Lattice via Helium Implantation, *Phys. Rev. Lett.*, 2015, **114**, 256801, DOI: **10.1103/PhysRevLett.114.256801**.

31 E. A. Kotomin and A. I. Popov, Radiation-induced point defects in simple oxides, *Nucl. Instrum. Methods Phys. Res., Sect. B*, 1998, **141**, 1–15, DOI: **10.1016/S0168-583X(98)00079-2**.

32 C. R. Kreller, *et al.*, Massively enhanced ionic transport in irradiated crystalline pyrochlore, *J. Mater. Chem. A*, 2019, **7**, 3917–3923, DOI: **10.1039/C8TA10967B**.

33 J. Wang, *et al.*, Tuning Point Defects by Elastic Strain Modulates Nanoparticle Exsolution on Perovskite Oxides, *Chem. Mater.*, 2021, **33**, 5021–5034, DOI: **10.1021/acs.chemmater.1c00821**.

34 S. Saremi, *et al.*, Local control of defects and switching properties in ferroelectric thin films, *Phys. Rev. Mater.*, 2018, **2**, 084414, DOI: **10.1103/PhysRevMaterials.2.084414**.

35 J. E. Fröch, *et al.*, Versatile direct-writing of dopants in a solid state host through recoil implantation, *Nat. Commun.*, 2020, **11**, 5039, DOI: **10.1038/s41467-020-18749-2**.

36 M. Zgirski, *et al.*, Ion beam shaping and downsizing of nanostructures, *Nanotechnology*, 2008, **19**, 055301, DOI: **10.1088/0957-4484/19/05/055301**.

37 J. F. Ziegler, M. D. Ziegler and J. P. Biersack, SRIM – The stopping and range of ions in matter, *Nucl. Instrum. Methods Phys. Res., Sect. B*, 2010, **268**, 1818–1823, DOI: **10.1016/j.nimb.2010.02.091**.

38 W. Jung and H. L. Tuller, A New Model Describing Solid Oxide Fuel Cell Cathode Kinetics: Model Thin Film SrTi1-xFexO3-δ Mixed Conducting Oxides–a Case Study, *Adv. Energy Mater.*, 2011, **1**, 1184–1191, DOI: **10.1002/aenm.201100164**.

39 E. Sediva, T. Defferriere, N. H. Perry, H. L. Tuller and J. L. M. Rupp, In Situ Method Correlating Raman Vibrational Characteristics to Chemical Expansion via Oxygen Nonstoichiometry of Perovskite Thin Films, *Adv. Mater.*, 2019, **31**, 1902493, DOI: **10.1002/adma.201902493**.

40 J. Wang, *et al.*, Fast Surface Oxygen Release Kinetics Accelerate Nanoparticle Exsolution in Perovskite Oxides, *J. Am. Chem. Soc.*, 2023, **145**, 1714–1727, DOI: **10.1021/jacs.2c10256**.

41 J. Wang, *et al.*, Exsolution-Driven Surface Transformation in the Host Oxide, *Nano Lett.*, 2022, **22**, 5401–5408, DOI: **10.1021/acs.nanolett.2c01439**.

42 N. W. Kwak, *et al.*, In situ synthesis of supported metal nanocatalysts through heterogeneous doping, *Nat. Commun.*, 2018, **9**, 4829, DOI: **10.1038/s41467-018-07050-y**.

43 Y.-R. Jo, *et al.*, Growth Kinetics of Individual Co Particles Exsolved on SrTi0.75Co0.25O3-δ Polycrystalline Perovskite Thin Films, *J. Am. Chem. Soc.*, 2019, **141**, 6690–6697, DOI: **10.1021/jacs.9b01882**.

44 J. K. Kim, *et al.*, Exceptional Tunability over Size and Density of Spontaneously Formed Nanoparticles via Nucleation Dynamics, *ACS Appl. Mater. Interfaces*, 2020, **12**, 24039–24047, DOI: **10.1021/acsami.0c05215**.

45 A. Nenning, *et al.*, The Electrochemical Properties of Sr(Ti,Fe)O3-δ for Anodes in Solid Oxide Fuel Cells, *J. Electrochem. Soc.*, 2017, **164**, F364–F371, DOI: **10.1149/2.1271704jes**.

46 T. Zhu, H. E. Troiani, L. V. Mogni, M. Han and S. A. Barnett, Ni-Substituted Sr(Ti,Fe)O3 SOFC Anodes: Achieving High Performance via Metal Alloy Nanoparticle Exsolution, *Joule*, 2018, **2**, 478–496, DOI: **10.1016/j.joule.2018.02.006**.

47 Y. Gao, *et al.*, Energetics of Nanoparticle Exsolution from Perovskite Oxides, *J. Phys. Chem. Lett.*, 2018, **9**, 3772–3778, DOI: **10.1021/acs.jpclett.8b01380**.

48 C. Wei-Su, W. Yang, G. Jun-Ming and H. Feng-Jiao, Thermal stability of Ni–Fe alloy foils continuously electrodeposited in a fluorborate bath, *Open J. Metal*, 2012, **2**, 18–23.

49 H. Han, *et al.*, Anti-phase boundary accelerated exsolution of nanoparticles in non-stoichiometric perovskite thin films, *Nat. Commun.*, 2022, **13**, 6682, DOI: **10.1038/s41467-022-34289-3**.

50 A. L. A. Marinho, *et al.*, Embedded Ni nanoparticles in CeZrO2 as stable catalyst for dry reforming of methane, *Appl. Catal., B*, 2020, **268**, 118387, DOI: **10.1016/j.apcatb.2019.118387**.

51 N. Kuganathan, F. Baiutti, A. Morata, A. Tarancon and A. Chroneos, Interstitial lithium doping in SrTiO3, *AIP Adv.*, 2021, **11**, 075029, DOI: **10.1063/5.0059306**.

52 S. J. Kim, T. Akbay, J. Matsuda, A. Takagaki and T. Ishihara, Strain Effects on Oxygen Reduction Activity of Pr2NiO4 Caused by Gold Bulk Dispersion for Low Temperature Solid Oxide Fuel Cells, *ACS Appl. Energy Mater.*, 2019, **2**, 1210–1220, DOI: **10.1021/acsaem.8b01776**.

53 J. Hyodo, K. Tominaga, J.-E. Hong, S. Ida and T. Ishihara, Effects of Three-Dimensional Strain on Electric Conductivity in Au-Dispersed Pr1.90Ni0.71Cu0.24Ga0.05O4 + δ, *J. Phys. Chem. C*, 2015, **119**, 5–13, DOI: **10.1021/jp504220y**.

54 Y. Shi, A. H. Bork, S. Schweiger and J. L. M. Rupp, The effect of mechanical twisting on oxygen ionic transport in solid-state energy conversion membranes, *Nat. Mater.*, 2015, **14**, 721–727, DOI: **10.1038/nmat4278**.

55 M. Kubicek, *et al.*, Tensile Lattice Strain Accelerates Oxygen Surface Exchange and Diffusion in La1–xSrxCoO3−δ Thin Films, *ACS Nano*, 2013, **7**, 3276–3286, DOI: **10.1021/nn305987x**.

56 D. Jennings, S. Ricote, J. Santiso, J. Caicedo and I. Reimanis, Effects of exsolution on the stability and morphology of Ni nanoparticles on BZY thin films, *Acta Mater.*, 2022, **228**, 117752, DOI: **10.1016/j.actamat.2022.117752**.

57 E. Fabbri and T. J. Schmidt, Oxygen Evolution Reaction—The Enigma in Water Electrolysis, *ACS Catal.*, 2018, **8**, 9765–9774, DOI: **10.1021/acscatal.8b02712**.

58 Z. W. Seh, *et al.*, Combining theory and experiment in electrocatalysis: Insights into materials design, *Science*, 2017, **355**, eaad4998, DOI: **10.1126/science.aad4998**.

59 Y.-C. Wang, *et al.*, Identification of the active triple-phase boundary of a non-Pt catalyst layer in fuel cells, *Sci. Adv.*, 2022, **8**, eadd8873, DOI: **10.1126/sciadv.add8873**.

60 C. B. Gopal and S. M. Haile, An electrical conductivity relaxation study of oxygen transport in samarium doped ceria, *J. Mater. Chem. A*, 2014, **2**, 2405–2417, DOI: **10.1039/C3TA13404K**.

61 B. Liu, H. Y. Xiao, Y. Zhang, D. S. Aidhy and W. J. Weber, Ab initio molecular dynamics simulations of threshold displacement energies in SrTiO3, *J. Phys.: Condens. Matter*, 2013, **25**, 485003, DOI: **10.1088/0953-8984/25/48/485003**.

62 Y. L. Huang, C. Pellegrinelli, K. T. Lee, A. Perel and E. D. Wachsman, Enhancement of La0.6Sr0.4Co0.2Fe0.8O3-δSurface

This journal is © The Royal Society of Chemistry 2023

Energy Environ. Sci., 2023, **16**, 5464–5478 | **5477**

Exchange through Ion Implantation, *J. Electrochem. Soc.*, 2015, **162**, F965–F970, DOI: **10.1149/2.1051508jes**.

63 J. Wang, *et al.*, Threshold catalytic onset of carbon formation on CeO2 during CO2 electrolysis: mechanism and inhibition, *J. Mater. Chem. A*, 2019, **7**, 15233–15243, DOI: **10.1039/C9TA03265G**.

64 J. Wang, K. B. Woller and B. Yildiz, Ion Beam as an External and Dynamic Metal Reservoir to Induce Nanoparticle Exsolution in Oxides, *ECS Trans.*, 2023, **111**, 809, DOI: **10.1149/11106.0809ecst**.

65 J. Wang, *et al.*, Strain-Dependent Surface Defect Equilibria of Mixed Ionic-Electronic Conducting Perovskites, *Chem. Mater.*, 2022, **34**, 5138–5150, DOI: **10.1021/acs.chemmater.2c00614**.

66 Y. Zhang, *et al.*, Ion-induced damage accumulation and electron-beam-enhanced recrystallization in SrTiO3, *Phys. Rev. B: Condens. Matter Mater. Phys.*, 2005, **72**, 094112, DOI: **10.1103/PhysRevB.72.094112**.

67 A. Ruosi, *et al.*, Electron sampling depth and saturation effects in perovskite films investigated by soft x-ray absorption spectroscopy, *Phys. Rev. B: Condens. Matter Mater. Phys.*, 2014, **90**, 125120, DOI: **10.1103/PhysRevB.90.125120**.

68 M. B. Stevens, *et al.*, Measurement Techniques for the Study of Thin Film Heterogeneous Water Oxidation Electrocatalysts, *Chem. Mater.*, 2017, **29**, 120–140, DOI: **10.1021/acs.chemmater.6b02796**.

5478 | *Energy Environ. Sci.*, 2023, **16**, 5464–5478

This journal is © The Royal Society of Chemistry 2023